Materials Research Proceedings **32** (2023) 253-263 https://doi.org/10.21741/9781644902615-29

Deformation behaviour and microstructural evolution of high-entropy CoFeMnNi alloy at hot deformation condition with low strain rate

Lihua Du[1,2,3,a*], Jiaai Shi[4,b], Jiayu Liang[4,c], Kailun Zheng[4,d]

[1] AVIC Manufacturing Technology Institute, Beijing 100024, China

[2]Aviation Key Laboratory of Science and Technology on Plastic Forming, Beijing 100024, China

[3]Beijing Key Laboratory on Digital Plastic Forming and Equipment, Beijing 100024, China

[4]Dalian University of Technology, Dalian 116024, China

[a,]quietness2007@126.com, [b]homura_zero@126.com,
[c]1262976726@qq.com,[d]zhengkailun@dlut.edu.cn

Keywords: High-Entropy Alloy, Deformation Behaviour, Super-Plastic Forming, Deformation

Abstract. High-entropy alloy is a promising structural material for high-temperature service applications due to the designable superior properties. Superplasticity, normally achieved at relatively high temperature and low strain rate, enables difficult to formation materials to manufacture complex-shaped parts. This paper presents a feasibility experimental study on the deformation and microstructure of CoFeMnNi high-entropy alloy under hot deformation conditions with low strain rate. A series of hot uniaxial tests were conducted at the temperature range between 800-1000℃ with typical strain rates of 10^{-4} and 10^{-5}/s to determine the stress-strain behaviours. Additionally, to understand the deformation mechanism, microstructure evolution after deformation was characterized. Finally, a mechanism based constitutive model of high-entropy alloy was developed, which facilities the process optimization by finite element simulations.

1. Introduction

The fabrication of High-entropy alloys (HEAs), featured by containing more than four to five major elements typically, is considered to be one of the greatest breakthroughs of alloy design [1]. Due to excellent properties such as high strength [2], excellent toughness [3] and wear resistance [4] for various extreme service environments, HEAs have attracted intensive research work in recent years. For further attempt to manufacture engineering parts, the investigation of deformation behaviour of HEAs is essential. HEAs are basically brittle at room temperature, with poor ductility and limited formability for further processing [5]. However, the ductility of HEA increases with the increase of processing temperature, which enable the various forming processes becomes possible.

Research on the formability of HEAs at elevated temperature has been carried out. Zhao et al. [6] manufactured CoCrFeNi HEA by laser powder-bed fusion technique and refined its grains, and the results show that the additive manufactured HEA has high strain hardening capability and increased plasticity. Stepanov et al. [7] investigated the characteristics of mechanical behaviour and microstructure evolution of AlCoCrCuFeNi HEA during superplastic rheology and found that the elongation of the HEA can reach 1240% at the temperatures of 800°C-1000°C and strain rates of 10^{-4}/s to 10^{-1}/s. Shahmir et al. [8] obtained CoCrFeNiMn HEA with a grain size of approximately 10nm by high-pressure torsion method, and found that the maximum elongation of HEA can exceed 600% at temperature of 973K. Li et al. [9] investigated the superplastic behaviour of CoCrFeNiCu HEA prepared by stir friction at the temperature of 900~950°C and the strain rate of 3×10^{-4}/s~3×10^{-2}/s and found that the friction stir processed CoCrFeNiCu HEA exhibited a maximum elongation of 620% and a flow stress of 5 MPa at the temperature of 950°C and the

strain of 3×10^{-3}/s. Li et al. [10] investigated the effects of annealing temperatures from 573 to 1373 K on the microstructure and mechanical properties of FeCoCrNiMn HEA produced by severe cold rolling with ultrafine structure, and found that the severe cold rolled HEA annealed at 923K and 973K has high strength–ductility combinations because of the formation of the fully recrystallized ultrafine-grained microstructure. However, most of the above investigations are based on highly cost consuming fabrication methods of HEAs. There are few investigations on deformation behaviour of HEAs fabricated by traditional process methods, which are more cost-effective for engineering application.

This paper presents a preliminary study on the new HEA CoFeMnNi under typical superplastic deformation conditions. The as-received material was extruded tube. Tensile specimens were machined from the initial extruded tubes, and a series of tensile tests at hot deformation condition with low strain rate were conducted. To reveal the underlying mechanisms, microstructural evolutions, including the average grain size, dislocation density and fracture morphology were also characterized. Finally, a mechanism-based material model of CoFeMnNi was established, which enables to predict both the macroscopic and microscopic variable evolutions.

2. Experimental method

The as-received material was extruded tube, from which the specimens used for characterizing the hot deformation behaviour of HEA were machined. Sub-sized specimen was machined along the extrusion direction from the tube, as schematically shown in Fig. 1. In the practical machining process, the extruded tube was firstly cut into columns with a fan ring cross-section and flattened to achieve rectangular sheets, and dog-bone shaped specimen was cut from the sheet.

A series of high temperature tensile tests were conducted investigate the formability of the CoFeMnNi alloy at the elevated temperature and low strain rate. Four deformation temperatures ranging from 850°C to 1000°C with a gap of 50°C and two strain rates, 0.0001/s and 0.00001/s were chosen for the tests.

After tensile tests, the fracture region A at the finer part of the specimen and the undeformed region B at the gripped part of the specimen were machined for EBSD observation to investigate the influence of the deformation on initial microstructure.

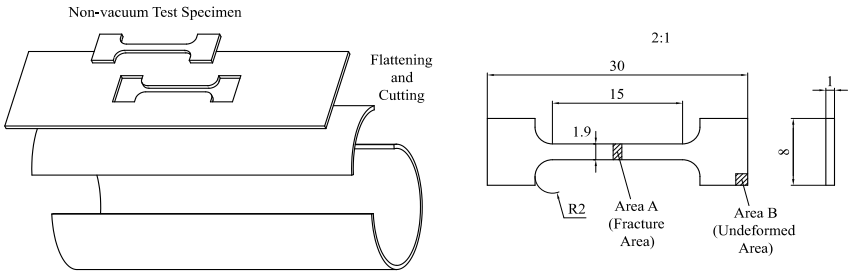

Fig. 1 *The schematic representation of specimen machining and dimensions of the specimen*

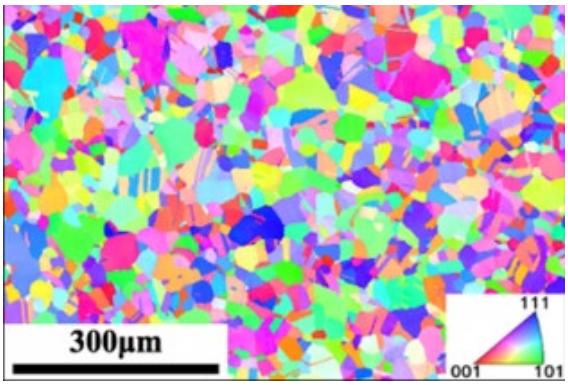

Fig. 2 *The as-received microstructure (with grain size of 6.13μm)*

3. Results of discussion

3.1 Stress-strain behaviours at hot deformation condition

Fig. 3 shows the true stress-strain curve of the CoFeMnNi HEA sheet specimen at different deformation conditions. Fig.3a showed that the true stress obviously increases by more than one-third with the strain rate increasing from 0.00001/s to 0.0001/s. Fig. 2b shows the temperature effect on the visco-plastic behavior at the strain rate of 0.0001/s, the value of the true stress obviously decreases as the temperature increases from 800°C to 1000°C. In addition, the plasticity of HEA is not uniform as the temperature increases evenly. When the temperature increases form 800°C to 850°C, the maximum true strain of the true stress-strain curve only slightly increases. As the temperature increases further, the maximum true strain of the true stress-strain curve increases sharply. When the temperature is 1000°C, the maximum true strain of the true stress-strain curve can be greater than 0.3, which means that the CoFeMnNi HEA has a relatively good plasticity at the temperature of 1000°C and may have acceptable formability to manufacture simple engineering parts.

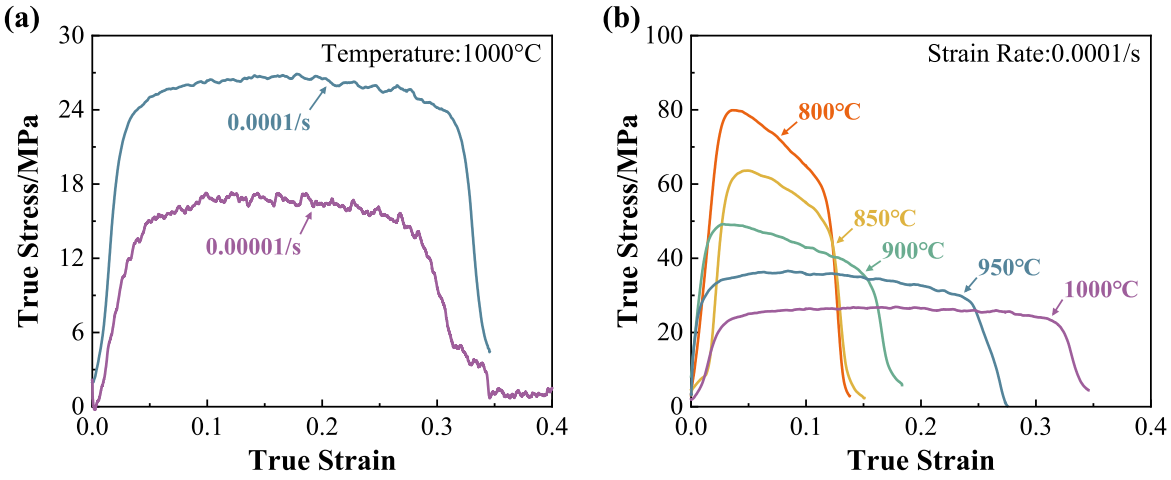

(a) Temperature of 1000°C (b) Strain Rate of 0.0001/s.

Fig. 3 *The true stress-strain curve of the CoFeMnNi HEA at the temperature of 1000°C and strain rate of 0.0001/s.*

3.2 EBSD Microstructure

3.2.1 Grain size and boundaries

Fig. 4 shows EBSD maps at various temperatures for fracture region A and undeformed region B, respectively. When deformation temperature ranged from 850°C to 950°C, the grain size of region A is slightly smaller than region B. Until the temperature was set to 1000°C, the grain size increased from 6.13 to 7.06μm. This phenomenon was attributed to refinement by the dynamic recrystallization during hot deformation. Regarding the same zones, as temperature increases, the grains tend to grow up for both the grains of region A and region B. However, the grain morphology at the region A have no obvious sign of uniaxial elongation and broadly remains isometric. In addition, as temperature increases from 850°C to 1000°C, the difference of the amount of twinning becomes more obvious. When the temperature is 1000°C, the amount of twinning is obviously less than that at the region B.

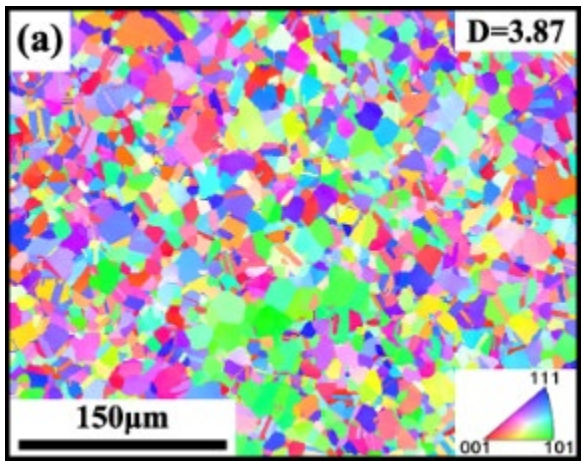

(a) 850°C-0.0001/s-region A

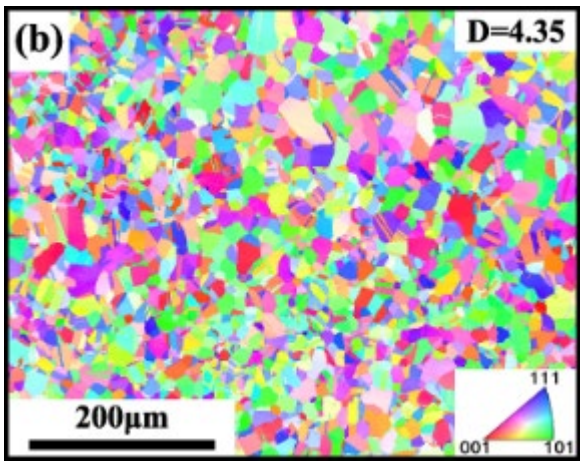

(b) 850°C-0.0001/s-region B

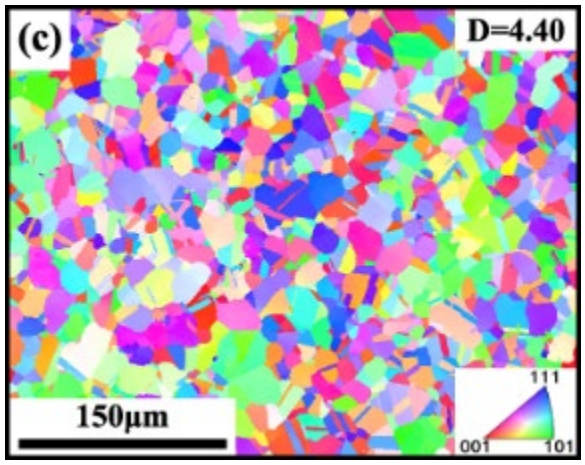

(c) 900°C-0.0001/s-region A

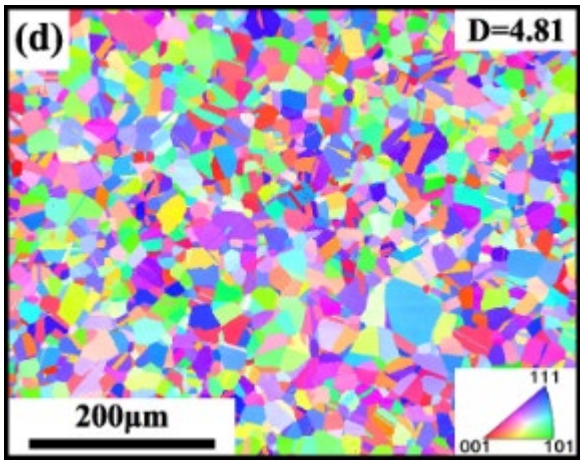

(d) 900°C-0.0001/s-region B

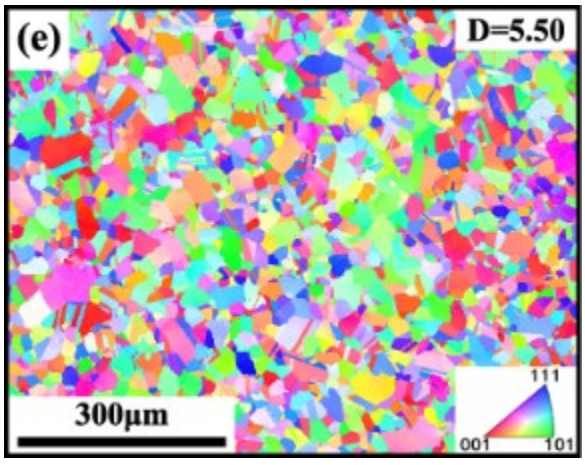

(e) 950°C-0.0001/s-region A

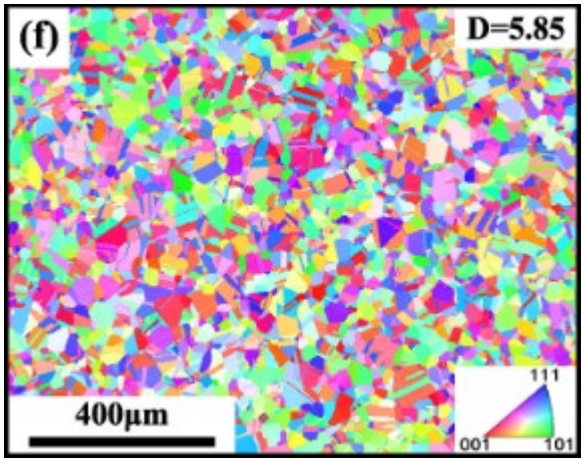

(f) 950°C-0.0001/s-region B

Materials Research Proceedings **32** (2023) 253-263 https://doi.org/10.21741/9781644902615-29

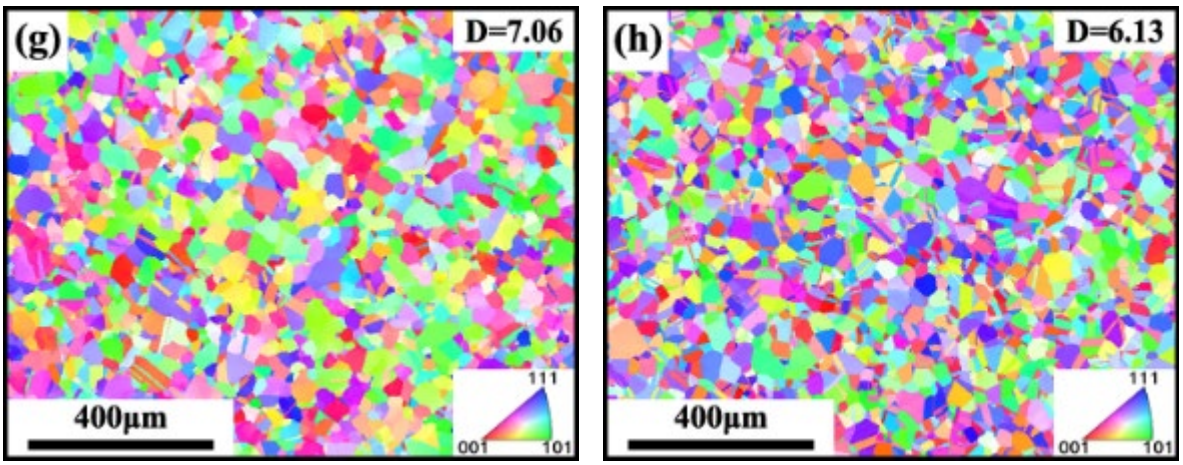

(g) 1000°C-0.0001/s-region A (h) 1000°C-0.0001/s-region B

Fig. 4 *The EBSD observations at different conditions and regions.*

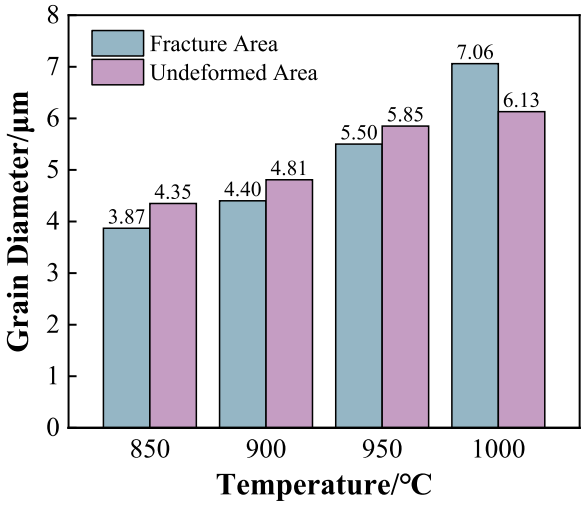

Fig. 5 *The calculated grain diameters under various temperatures and at different regions.*

The obtained EBSD grain boundary maps at various temperatures are shown in Fig. 6. The grain boundaries, indicated by red, green and blue relatively means the angle of the grain boundaries are relatively ranged from 2° to 5°, from 5° to 15° and from 15° to 180°. The results shows that the angle of majority of the grain boundaries ranges from 15° to 180° for whole temperature range and both two regions. It is indicated that grain boundary sliding dominates the deformation rather than the dislocation motion mechanism.

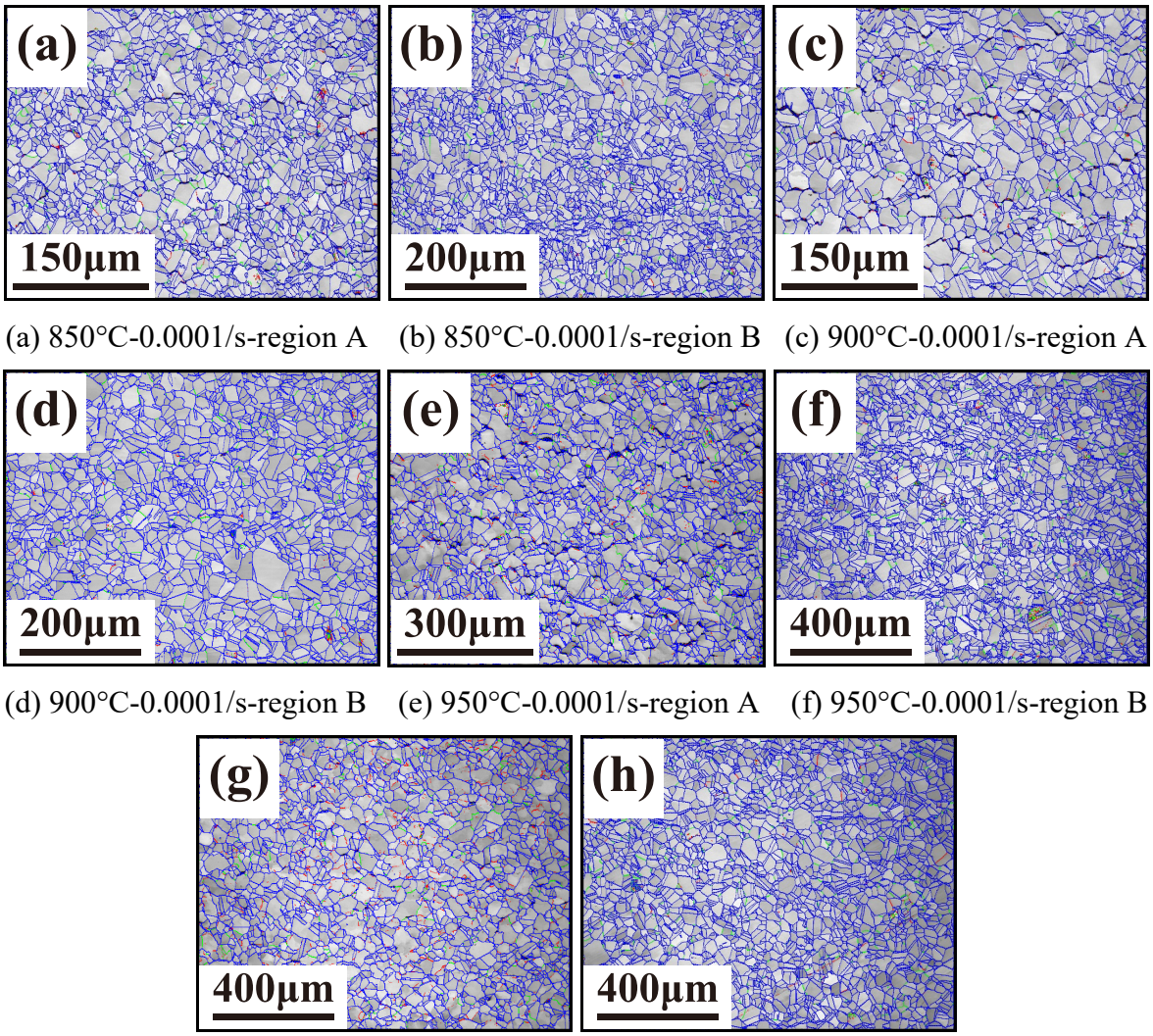

(a) 850°C-0.0001/s-region A (b) 850°C-0.0001/s-region B (c) 900°C-0.0001/s-region A

(d) 900°C-0.0001/s-region B (e) 950°C-0.0001/s-region A (f) 950°C-0.0001/s-region B

(g) 1000°C-0.0001/s-region A (h) 1000°C-0.0001/s-region B

Fig. 6 *The grain boundary map at different condition and different region.*

Fig. 7 summarises the quantification of the fractions of the grain boundaries with different angles at various temperatures for two regions. For the high-angle grain boundary fraction, as temperature increases from 850°C to 1000°C, the fraction of the grain boundaries (>15°) gradually decreases in both fracture region and undeformed region. In addition, the decline magnitude of the fraction of the grain boundaries (>15°) is obviously larger than that at the undeformed region as the temperature increases from 900°C to 1000°C. However, when the temperature is 1000°C, the fraction of the grain boundaries (>15°) in both fracture region and undeformed region can still be larger than 0.85. The fraction of the grain boundaries (5°-15°) has no significant changes as the temperature increases from 850°C to 1000°C. However, the fraction of the grain boundaries (2°-5°) has different variation trends as the temperature from 850°C to 1000°C. In the fracture region, the fraction of the grain boundaries (2°-5°) obviously increases. However, for the undeformed region, the fraction of the grain boundaries (2°-5°) has no significant change as the temperature increases from 850°C to 1000°C.

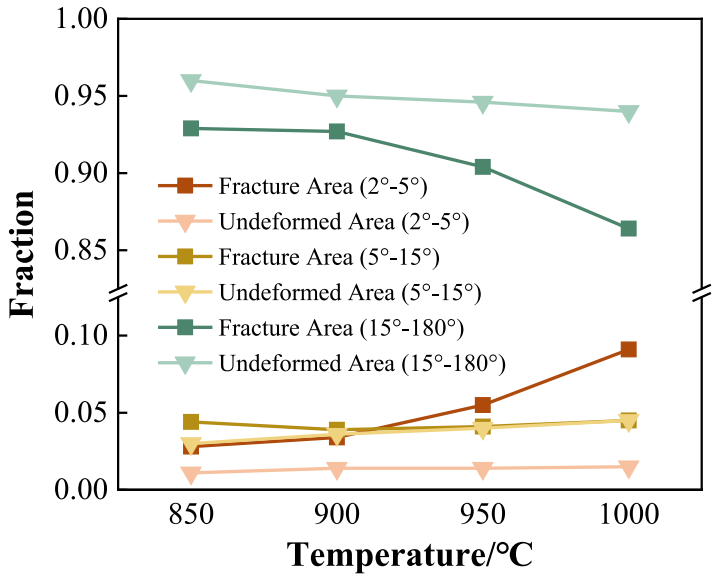

***Fig.** 7 The fraction of grain boundaries with different angles at various temperatures in fracture and undeformed regions, respectively*

3.3 Visco-plastic constitutive modelling

3.3.1 Material modelling

In order to characterize the hot flow behaviour of HEA, constitutive modelling to model the stress-strain at hot deformation behaviour with low strain rate is essential. In addition, to realize the overall prediction of microstructure evolutions, mechanism-based modelling scheme is used in this paper. The complete equation set is summarized using Eqs. (1) to (8):

Equation (1) is the generalized visco-plastic flow law expressed in the form of rate. For visco-plastic deformation, the strain rate equation is established considering the strain-hardening behavior at the beginning of the deformation and the microstructure evolution, e.g. grain size evolution, during the hot straining.

$$\dot{\varepsilon}^P = \left(\frac{\frac{\sigma}{(1-\omega_{1D})} - R - k}{K} \right)^{n_1} \left(\bar{d}\right)^{-u} \tag{1}$$

where, $\dot{\varepsilon}^p$ is the plastic strain rate, σ is the equivalent force, R is the hardening-related hardening state variable, k is the initial yield stress (critical stress), which is temperature-dependent, K and n_1 are temperature-dependent coefficients, μ is a constant, and $\bar{d}$ is the average grain size. In addition, the equations take into account the damage and grain size evolution during thermal deformation by introducing the normalized grain size $\bar{d}$ and the one-dimensional damage ω_{1D}.

Equation (2) is the dislocation density rate equation composed by three terms. The first term describes the dislocation density accumulation and dynamic recovery in plastic deformation, while the second and third terms consider the effect of static recovery and dynamic recrystallization on the evolution of dislocation density, respectively. Usually, the dislocation density tends to increase, then decrease, and then becomes a saturated state. At the beginning of the material deformation, strain hardening causes the dislocation density to increase, and after the deformation proceeds to a certain extent, dynamic reversion and other effects cause the dislocation density to decrease, and at the end of the deformation, the dislocation density tends to stabilize.

$$\dot{\rho} = A(1-\bar{\rho})|\dot{\varepsilon}^P| - C_1\dot{\bar{\rho}}^{n_2} - [C_2\bar{\rho}/(1-S)]\dot{S} \tag{2}$$

where, A, C_1 are temperature dependent coefficients and C_2 is a constant.

Materials Research Proceedings **32** (2023) 253-263 https://doi.org/10.21741/9781644902615-29

Equation (3) is the critical dislocation density equation, which can be used to determine the moment when recrystallization occurs during the deformation of a high-entropy alloy, i.e., when the dislocation density value is higher than the critical dislocation density, the material recrystallizes.

$$\bar{\rho}_c = q_3 \dot{\varepsilon}^{q_4} \tag{3}$$

where, q_3 and q_4 are temperature-dependent coefficients.

Equation (4) is the hardening rate equation, which describes the evolution of the hardening behavior of the material. The hardening of the material is determined by the dislocation density, which increases monotonically to saturation, and is directly related to the plastic strain because recrystallization and annealing are not considered in the effect on hardening at the beginning of the high temperature deformation process.

$$\dot{R} = 0.5 b \bar{\rho}^{-0.5} \dot{\bar{\rho}} \tag{4}$$

where, B is the temperature-dependent coefficient and $\bar{\rho}$ is the normalized dislocation density of the material, which is 0 at the beginning of the deformation and increases with the deepening of the deformation until it reaches 1 at saturation.

Equation (5) is the recrystallization evolution equation, the recrystallization coefficient is maximum from 0 to 1. During recrystallization, new grains are nucleated and the total number of grains increases. During thermal deformation, dislocation accumulation leads to slip and shear at grain boundaries. In addition, the occurrence of dynamic recrystallization leads to the creation of new grains, which reduces the average grain size and can even reduce the rate of dislocation accumulation and dislocation density.

$$\dot{S} = \frac{q_1 (0.1 + S)^{q_2} (1 - S) \bar{\rho}^2}{\bar{d}} \tag{5}$$

where, q_1 and q_2 are both temperature-dependent equation coefficients.

Equation (6) is the grain evolution equation, which consists of three terms, where the first term represents the static grain growth during thermal deformation, which is determined by the migration and energy density of grain boundaries; the second term describes the plastic strain leading to grain evolution, and the third term represents the combined effect of recrystallization leading to grain refinement and strain rate.

$$\dot{d} = w_1 d^{-\gamma_1} + w_2 \dot{\varepsilon}^{-\gamma_2} - w_3 \dot{S}^{\gamma_3} \left(\bar{d}\right)^{\gamma_4} \tag{6}$$

where, w_1 and w_2 are material constants related to grain mobility and grain boundary energy density. w_3 is a temperature dependent coefficient, andγ_1, γ_2, γ_3 and γ_4 are constants.

Equation (7) is the damage rate equation. The damage equation was established based on the continuous damage mechanism and the superplastic forming model.

$$\dot{\omega} = \left[\frac{\eta_1}{(1-\omega)^{\eta_3}} (\dot{\varepsilon}^P)^{\eta_2}\right](1 - \delta) + \left[\eta(1 - \xi)\dot{\varepsilon}_P + \frac{F \varepsilon^p}{(1 - \xi)} \sigma \dot{\varepsilon}_P\right] \tag{7}$$

where, ω denotes the region fraction of the damaged material and ranges from 0 to 1. the damage value $\dot{w} = 0$ is the initial state of the material, and failure is assumed to occur when $\dot{w}$ reaches 0.7. η_1, η_2, η_3 are temperature-dependent coefficients.

Equation (8) is a one-dimensional stress equation considering damage.

$$\sigma = E(1 - \omega)(\varepsilon^T - \varepsilon^P) \tag{8}$$

where, E is Young's modulus, ε^T is the total strain, and ε^P is the plastic strain.

For the temperature dependent coefficients, the equations are summarized in Table 2.

Materials Research Proceedings **32** (2023) 253-263 https://doi.org/10.21741/9781644902615-29

Table 2 *Temperature dependent material coefficient equations*

$K = K_0 exp\ (\frac{QK_0}{RT})$	$k = k_0 exp\ (\frac{Qk_0}{RT})$	$n_1 = n_{10}\exp\ (\frac{Qn_{10}}{RT})$
$A = A_0 exp\ (\frac{QA_0}{RT})$	$B = B_0 exp\ (-\frac{QB_0}{RT})$	$W_1 = W_{10} exp\ (-\frac{QW_{10}}{RT})$
$q_1 = q_{10} exp\ (\frac{Qq_{10}}{RT})$	$q_2 = q_{20} exp\ (\frac{Qq_{20}}{RT})$	$W_2 = W_{20} exp\ (-\frac{QW_{20}}{RT})$
$q_4 = q_{40}\exp\ (\frac{Qq_{40}}{RT})$	$q_3 = q_{30}\exp\ (\frac{Qq_{30}}{RT})$	$W_3 = W_{30} exp\ (-\frac{QW_{30}}{RT})$
$\gamma_1 = \gamma_{10} exp\ (\frac{-Q\gamma_{10}}{RT})$	$\gamma_2 = \gamma_{20} exp\ (\frac{Q\gamma_{20}}{RT})$	$\eta_1 = \eta_{10} exp\ (\frac{Q\eta_{10}}{RT})$
$\gamma_3 = \gamma_{30} exp\ (\frac{-Q\gamma_{10}}{RT})$	$\gamma_4 = \gamma_{40} exp\ (\frac{Q\gamma_{40}}{RT})$	$C_1 = C_{10} exp\ (\frac{-QC_{10}}{RT})$
$C_2 = C_{20} exp\ (\frac{-QC_{20}}{RT})$	$E = E_0 exp\ (\frac{QE_0}{RT})$	$P = P_1 \cdot \dot{\varepsilon}_P^2 + P_2 \cdot \dot{\varepsilon}_P + P_3$
$F = \dot{\varepsilon}_p^{0.4}$		

3.3.2 Model prediction accuracy

Figure 7 compares the hot deformation behaviour between the model predictions (scattered points) and experimental results (solid line). The material constants were determined by trial & error fitting, which are given in Table 3.

Table 3 *Coefficient of CoFeMnNi high entropy alloy material model equation*

Parameter	K_0	k_0	n_{10}	E_0	B_0
Value	800	0.002265	2.56	258.5	0.5
Parameter	QK_0	Qk_0	Qn_{10}	QE_0	QB_0
Value	-1.84e-07	6.78E+04	0.0002122	1.67E+04	9.43E-05
Parameter	A_0	C_{10}	C_{20}	W_{10}	W_{20}
Value	4.43	0.0982	6.8	4.62E-4	0.0053
Parameter	QA_0	QC_{10}	QC_{20}	QW_{10}	QW_{20}
Value	0.0002424	-4.29E-05	0.000241	0.1622	4.0107E-04
Parameter	W_{30}	q_{10}	q_{20}	q_{30}	q_{40}
Value	2860	0.3	0.3	0.154	0.268
Parameter	QW_{30}	Qq_{10}	Qq_{20}	Qq_{30}	Qq_{40}
Value	1.14E-0	6.26E-05	6.26E-05	-2.09E-06	2.92E-05
Parameter	γ_1	γ_2	γ_3	γ_4	η_1
Value	3.073126	2.088153	2	2	0.01523
Parameter	$Q\gamma_{10}$	$Q\gamma_{20}$	$Q\gamma_{30}$	$Q\gamma_{40}$	$Q\eta_{10}$
Value	-4.73E-06	1.22E-04	3.11E-04	3.11E-04	1.27E+04
Parameter	η_2	η_3	R	U	
Value	1.452	24.9	8.314	6	
Parameter	$Q\eta_{20}$	$Q\eta_{30}$			
Value	-3537	1.48E-05			

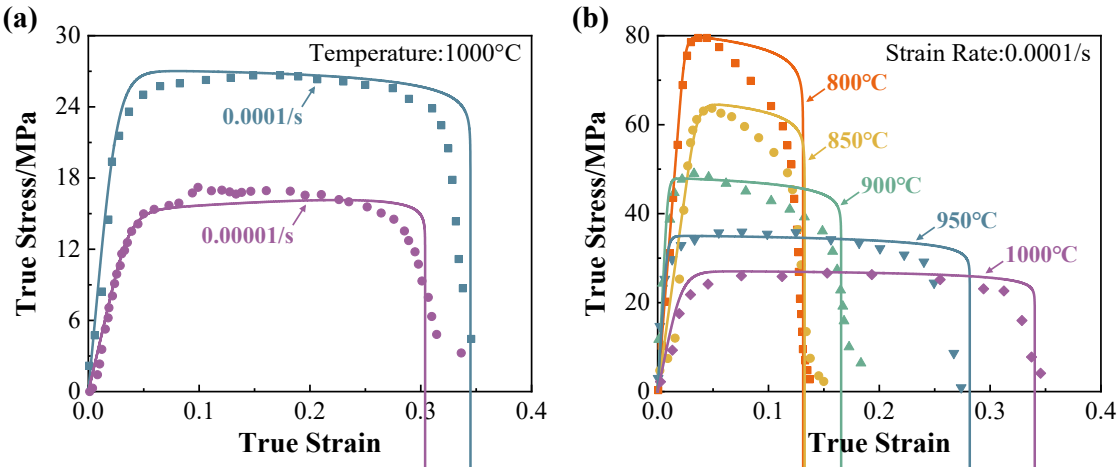

(a) Temperature of 1000° C (b) Strain Rate of 0.0001/s

***Fig.7** Comparison of experimental results and model prediction of hot flow behaviour of CoFeMnNi high entropy alloy under compression*

The overall prediction of the fitted stress-strain curves for the hardening (dislocation accumulation) and softening (dynamic recrystallization) under different conditions is in relatively good agreement. The accuracy of the predictions of the developed high-temperature alloy model was verified by Pearson's correlation coefficient (Person's R), and the equation is shown in (9):

$$R = \frac{\sum_{i=1}^{N}(\sigma_E - \bar{\sigma}_E)(\sigma_p - \bar{\sigma}_p)}{\sqrt{\sum_{i=1}^{N}(\sigma_E - \bar{\sigma}_E)^2 \sum_{i=1}^{N}(\sigma_p - \bar{\sigma}_p)^2}} \tag{9}$$

where, σ_E and σ_P are the experimental stress value and predicted stress value, $\bar{\sigma}_E$ and $\bar{\sigma}_P$ are the mean experimental stress value and the mean predicted stress value, and N is the number of data points. The calculated R value indicates the comparison accuracy, and the R value ranges from 0 to 1, where the closer the R value is to 1, the higher the prediction accuracy of the model. From the calculations, it can be concluded that the average R-values are 0.99689 and 0.9904 for different temperatures and different strain rates, respectively, which means that the prediction accuracy of the model is 99%.

In addition, the prediction error of the model can be quantified by the absolute mean error AARE. The equation is given in (10):

$$AARE = \frac{1}{N}\sum_{i=1}^{N}\left|\frac{\sigma_E - \sigma_p}{\sigma_E}\right| \times 100\% \tag{10}$$

where E is the experimental stress value, P is the stress value predicted by the model, and N is the number of experiments used in the calculation. The AARE values shown in figures (a) and (b) are 0.03789 and 0.08453, respectively, which implies a maximum average relative error of 8.45%.

Conclusion

1) The stress-strain curves of CoFeMnNi HEA under hot conditions with low strain rate exhibited typical visco-plastic deformation behaviour. The ductility increase was not uniform with the deformation temperature increases from 850°C to 1000°C. When the temperature was set to 1000

℃ further, the maximum of the true strain (slightly larger than 0.3) was achieved, which means that the material exhibited relatively good feasibility at such deformation condition.
2) EBSD observation results showed that the average grain size of HEAs slightly decreased after hot deformation at the temperatures ranging from 850°C to 950°C, which means the grain size was much more stable compared to typical titanium alloys deformed at hot deformation with low strain rate. Until the deformation temperature reached 1000 ℃, the grain size increased by 15% approximately.
3) A mechanism based hot deformation constitutive model of high entropy alloy was developed. Acceptable agreements between experimental and calculation results were achieved.

References

[1] Yeh J.W. Alloy design strategies and future trends in high-entropy alloys[J]. Jom, 2013, 65: 1759-1771. https://doi.org/10.1007/s11837-013-0761-6

[2] Ye Y.F. Wang Q, Lu J, et al. High-entropy alloy: challenges and prospects[J]. Materials Today, 2015, 19(6). https://doi.org/10.1016/j.mattod.2015.11.026

[3] Zhao S., Li Z., Zhu C. et al. Amorphization in extreme deformation of the CrMnFeCoNi high-entropy alloy[J]. Science advances, 2021, 7(5): eabb3108 https://doi.org/10.1126/sciadv.abb3108

[4] Zhang Y., Zuo T. T, Tang Z., et al. Microstructures and properties of high-entropy alloys[J]. Progress in materials science, 2014, 61: 1-93. https://doi.org/10.1016/j.pmatsci.2013.10.001

[5] D. B. Miracle and O. N. Senkov. A critical review of high entropy alloys and related concepts[J]. Acta Materialia, vol. 122, pp. 448-511, 2017/01/01/ 2017. https://doi.org/10.1016/j.actamat.2016.08.081

[6] W. Zhao et al. Significance of grain refinement on micro-mechanical properties and structures of additively-manufactured CoCrFeNi high-entropy alloy[J]. Materials Science and Engineering A, vol. 807, 202 https://doi.org/10.1016/j.msea.2021.140898

[7] N.D. Stepanov, D.G. Shaysultanov, G.A. Salishchev, O.N. Senkov, Mechanical behavior and microstructure evolution during superplastic deformation of the fine-grained AlCoCrCuFeNi high entropy alloy[J]. Materials Science Forum, 1662-9752, Vols. 838-839, pp 302-30 https://doi.org/10.4028/www.scientific.net/MSF.838-839.302

[8] H. Shahmir, J. He, Z. Lu, M. Kawasaki, and T. G. Langdon. Evidence for superplasticity in a CoCrFeNiMn high-entropy alloy processed by high-pressure torsion[J]. Materials Science and Engineering: A, vol. 685, pp. 342-348, 2017/02/08/ 2017. https://doi.org/10.1016/j.msea.2017.01.016

[9] N. Li et al. Achieving superior superplasticity in CoCrFeNiCu high entropy alloy via friction stir processing with an improved convex tool[J]. Materials Science and Engineering A, vol. 873, 2023. https://doi.org/10.1016/j.msea.2023.145034

[10] Z. Li et al. Effect of Annealing Temperature on Microstructure and Mechanical Properties of a Severe Cold-Rolled FeCoCrNiMn High-Entropy Alloy[J]. Metallurgical and Materials Transactions A: Physical Metallurgy and Materials Science, vol. 50, no. 7, pp. 3223-3237, 2019. https://doi.org/10.1007/s11661-019-05231-y

[11] J.G. Lin. Fundamentals of materials modelling for metals processing technologies: theories and applications[M]. Changsha, China: Central South University Press, 2019.